RSC Advances

ROYAL SOCIETY OF CHEMISTRY

www.rsc.org/advances

RSC Advances

RSCPublishing

ARTICLE

Tin Antimony Alloy-Filled Porous Carbon Nanofiber Composite for Use as Anode in Sodium-Ion Batteries

Cite this: DOI: 10.1039/x0xx00000x

Chen Chen[a], Kun Fu[a], Yao Lu[a], Jiadeng Zhu[a], Leigang Xue[a], Yi Hu[b], Xiangwu Zhang[a],*

Received 00th January 2012,
Accepted 00th January 2012

DOI: 10.1039/x0xx00000x

www.rsc.org/

Abstract

Lithium-ion battery is currently the dominate energy storage technology for electronic devices and electric vehicles. However, the predictable rising cost of lithium raw materials results in increasing interests in less expensive rivals, such as sodium-ion battery. In this work, tin antimony (SnSb) alloy-filled porous carbon nanofiber composite was prepared as a sodium-ion battery anode material by a simple electrospinning method with subsequent thermal treatment. The spinning solution contained antimony tin oxide nanoparticles as the SnSb alloy precursor, polyacrylonitrile as the carbon precursor, and polymethyl methacrylate (PMMA) as the pore generator. The resultant SnSb/C nanofiber composite formed a continuous conductive network, which was favorable for enhancing the electrochemical performance. The presence of SnSb alloy significantly increased the energy storage capacity of the composite due to its high theoretical capacity. The porous structure created by the decomposition of PMMA polymer provided free space to buffer the volume change of the SnSb alloy during the sodiation-desodiation process. The resultant SnSb@C nanofiber composite exhibited high capacity and stable rate capability, and was demonstrated to be a promising anode candidate for sodium-ion batteries.

Introduction

Since Sony produced the first commercial lithium-ion battery in the early 1990's, the characteristics of high energy density, no memory effect, and long lifespan make lithium-ion batteries the most used energy storage system in various applications such as portable electronics including laptops, cellphones, electric vehicles and hybrid electric vehicles. [1,2] However, considering the limited lithium source on earth and the continuously increasing energy demand, other

feasible energy storage technologies must be developed to resolve the foreseeable cost issue of lithium-ion batteries.[3] As an alternative material, sodium possesses similar chemical properties to lithium, but has lower cost and higher abundance. Hence, using the same mechanism and similar material structures, low-cost sodium-ion batteries can be developed for large-scale applications. [4]

So far, sodium-ion battery research mainly focused on cathode materials including $NaVPO_4F$,[5] $Na_{0.44}MnO_2$,[6] $Na_{0.85}Li_{0.17}Ni_{0.21}Mn_{0.64}O_2$,[7] *etc.*. Compared with the development of cathode materials, fewer studies were performed on the development anode materials. Graphite, a commercial anode material in lithium-ion batteries, was first studied for use as sodium-ion battery anode, but it was difficult for sodium ions to intercalate into the basal planes of graphite.[8,9] Other carbonaceous materials have also been studied as sodium-ion battery anodes. For example, the nitrogen-doped porous carbon fibers prepared by Yan *et al.*[10] showed a reversible capacity of around 230 mAh g^{-1} with good rate performance, and a template carbon produced by Philipp *et al.*[11] exhibited a reversible capacity of around 140 mAh g^{-1} in 40 cycles. One major disadvantage of these carbonaceous anode materials are their relatively low capacities. Tin (Sn) and antimony (Sb) based materials have been widely investigated as lithium-ion battery anodes due to their high theoretical capacities (993 mAh g^{-1} for Sn and 660 mAh g^{-1} for Sb).[12–15] Analogously, sodium ions are also found to be able to intercalate with Sn and Sb to form sodium alloys in a similar way with lithium alloys, producing theoretical capacities of 847 mAh g^{-1} ($Na_{15}Sn_4$) and 660 mAh g^{-1} (Na_3Sb) for Sn and Sb, respectively.[16] For example, Takayuki Yamamoto *et al.*[17] prepared Sn electrodes and achieved a high initial capacity of 790 mAh g^{-1}. But the capacity reduced quickly to only 150 mAh g^{-1} after 30 cycles. In lithium-ion batteries, the rapid capacity decay of Sn and Sb based anodes is typically ascribed to the large volume changes of Sn and Sb particles during the lithiation-delithiation process. Such volume change leads to the pulverization of electrodes, which in turn causes the breakdown of electric conductive network and insulation of the active material.[18] As sodium ions have larger radius

than lithium ions, even larger volume changes can be predicted in the sodiation-desodiation process when Sn and Sb are used as the anode materials in sodium-ion batteries. Therefore, the technological impact of developing alloy-based sodium-ion anode materials with stable structure and excellent cycling behavior would be significant and needs further exploration.

In this article, we report a Sn/Sb alloy nanoparticle-filled porous carbon (SnSb@C) nanofiber composite produced by an inexpensive electrospinning approach with subsequent thermal treatment. Figure 1 illustrates schematically the preparation procedure of the SnSb@C nanofiber composite. Electrospun composite nanofibers were first prepared using a mixed solution, containing antimony tin oxide (ATO) nanoparticles as the SnSb alloy precursor, polyacrylonitrile (PAN) as the carbon precursor, and polymethyl methacrylate (PMMA) as the pore generator. These electrospun precursor nanofibers were then thermally-treated to form the SnSb@C nanofiber composite structure, during which ATO was reduced to SnSb alloy, PAN was converted to carbon matrix, and PMMA was completely decomposed to form a porous architecture inside the nanofibers. The electrochemical performance, including specific capacity, cycling stability, and rate capability, of the SnSb@C nanofiber composite was evaluated by galvanostatic charge-discharge tests. The results demonstrated that the carbon nanofiber matrix and the porous architecture work synthetically to buffer the volume change of the SnSb alloy during the sodiation-desodiation process, leading to high capacity, good cycling performance, and high rate capability of the SnSb@C nanofiber composite anode.

Experimental

Chemicals

Polyacrylonitrile (PAN, average Mw = 150,000, Aldrich), polymethyl methacrylate (PMMA, average Mw = 120,000, Aldrich), antimony tin oxide (SnO_2/Sb_2O_5, ATO, particle diameter < 50 nm, Aldrich), N,N-dimethylformamide (DMF, 99.8%, Aldrich),

dimethyl carbonate (DMC, ⩾ 99 %, Aldrich), ethylene carbonate (EC, 98 %, Aldrich), sodium (Na, Aldrich), sodium perchlorate ($NaClO_4$, 98 %, Aldrich) were purchased from Sigma-Aldrich Chemical Company (USA) and were used without further purification.

Nanofiber Preparation

PAN solution (8%) in DMF was prepared by vigorous mechanical stirring for 5h at 60 °C. ATO nanoparticles (ATO:PAN = 1:1, 0.5:1, and 0:1 by weight) and PMMA polymer (PMMA:PAN = 1:10 by weight) were then added into the PAN solution and vigorously stirred for 24 h at room temperature to obtain homogeneous dispersions for electrospinning.

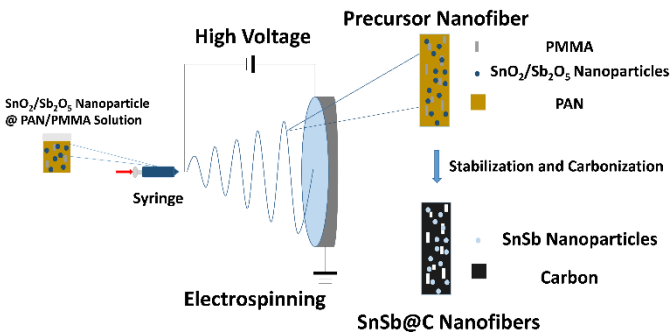

Figure 1. Schematic for preparation of SnSb@C nanofiber composite.

Precursor nanofibers were prepared by electrospinning with an applied voltage of 15 kV, a solution flow rate of 0.75 mL/h, and a needle tip-to-collector distance of 15 cm. To form SnSb@C nanofiber composites, electrospun precursor nanofibers were first stabilized in air at 280 °C for 5.5 h with a heating rate of 5 °C/min and then carbonized at 700 °C in argon for 3 h with a heating rate of 2 °C/min. During this process, PAN was converted to form the carbon nanofiber matrix and ATO was reduced to SnSb alloy nanoparticles while PMMA was decomposed completely, resulting in the formation of a porous structure within the carbon matrix.

Structural Characterization

The XRD analysis was conducted using a Rigaku SmartLab X-ray diffractometer with Cu Kα radiation between 2θ angles from 20° to 70°. Field-emission scanning electron microscopy (FESEM, JEOL 6400) and field-emission transmission electron microscopy (FETEM, Hitachi HF2000) were employed to characterize the morphology of precursor nanofibers and SnSb@C nanofiber

composites. Thermal gravimetric analysis (Perkin Elmer Pyris 1 TGA) and CHN elemental analysis were conducted to examine the compositions of SnSb@C nanofiber composites.

Electrochemical Evaluation

SnSb@C nanofibers (80 wt. %) were ground into the powder form and mixed with carbon black (10 wt. %) and alginic acid sodium salt (10 wt. %) to form a homogeneous slurry with deionized water as the solvent. The slurry was then pasted on a copper foil, followed by drying in a vacuum oven for 24 hours. CR2032-type coin cells were assembled in an argon-filled glove box using sodium metal as the counter electrode and a microporous glass fiber membrane (Whatman) as the separator. The electrolyte used in this study was 1M $NaClO_4$ in a solvent of ethylene carbonate and diethyl carbonate (EC/DEC, 1:1 by volume).

Cyclic Voltammetry (CV) measurements were performed by Gamry Reference 600 Potentiostat/Galvanostat/ZRA system in a voltage range of 2.5 to 0.01 V with a scan rate of 0.05 mV s^{-1}. Galvanostatic charge–discharge tests were conducted using LAND CT2001A battery testing system in a voltage range of 0.01 to 2.5 V. The capacity values were calculated based on the total composite weight.

Results and Discussion

Structure Characterization

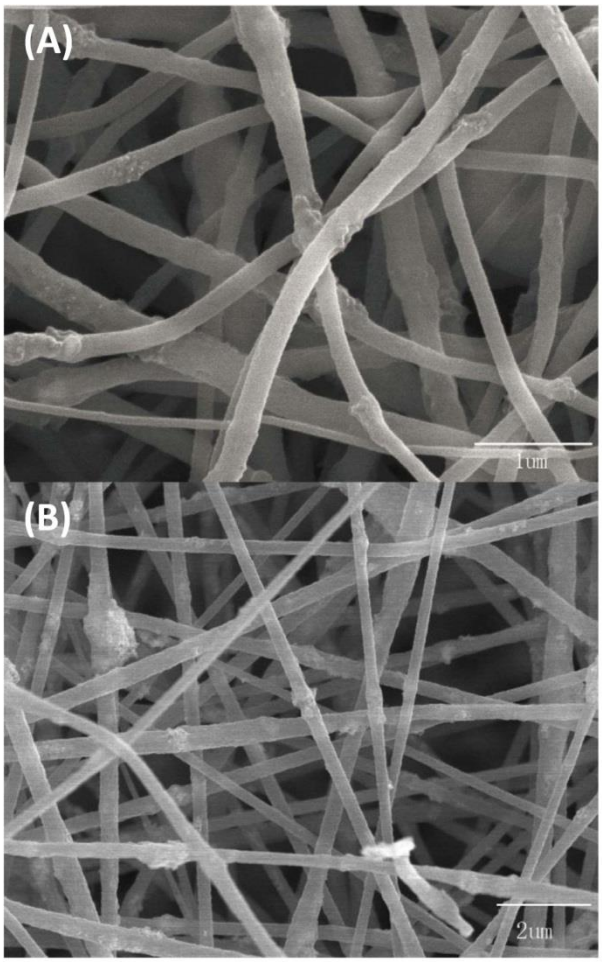

Figure 2. SEM images of ATO@PAN/PMMA nanofibers with ATO:PAN ratio of 0.5:1.

Figure 2 shows the SEM images of electrospun precursor nanofibers with an ATO:PAN weight ratio of 0.5:1. It is seen that the as-spun precursor nanofibers are continuous and have relatively uniform diameters. A few knob-like structures are detected from the surface of the nanofibers, which can be attributed to the agglomeration of ATO nanoparticles.

Figure 3 shows SEM images of SnSb@C nanofibers carbonized from precursor with ATO:PAN ratio of 0.5:1. Similar to the precursor nanofibers, SnSb@C nanofibers also form a three-dimensional network structure. A few knots, representing the aggregation of the nanoparticles, can still be detected. TEM images of these SnSb@C nanofibers are shown in Figure 4.

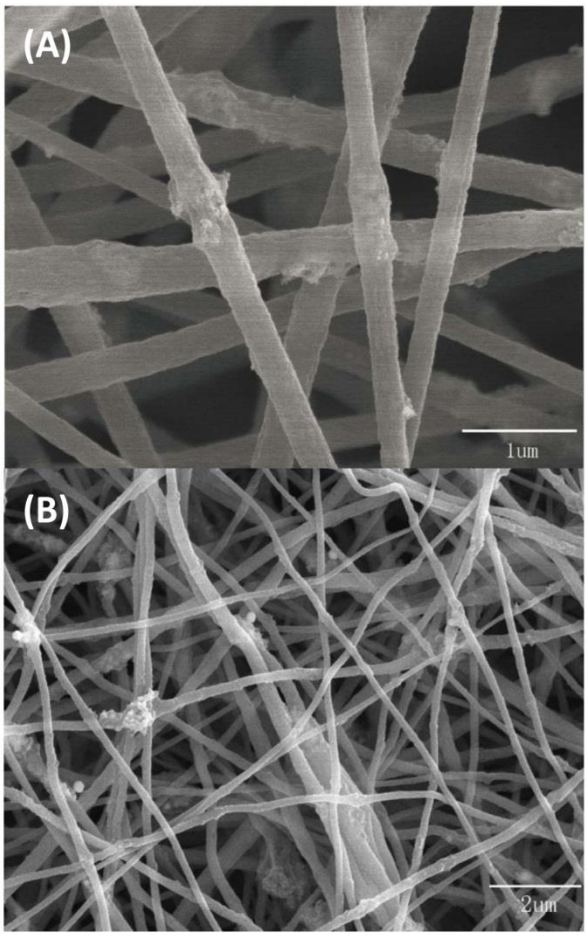

Figure 3. SEM images of SnSb@C nanofibers prepared from precursor with ATO:PAN ratio of 0.5:1.

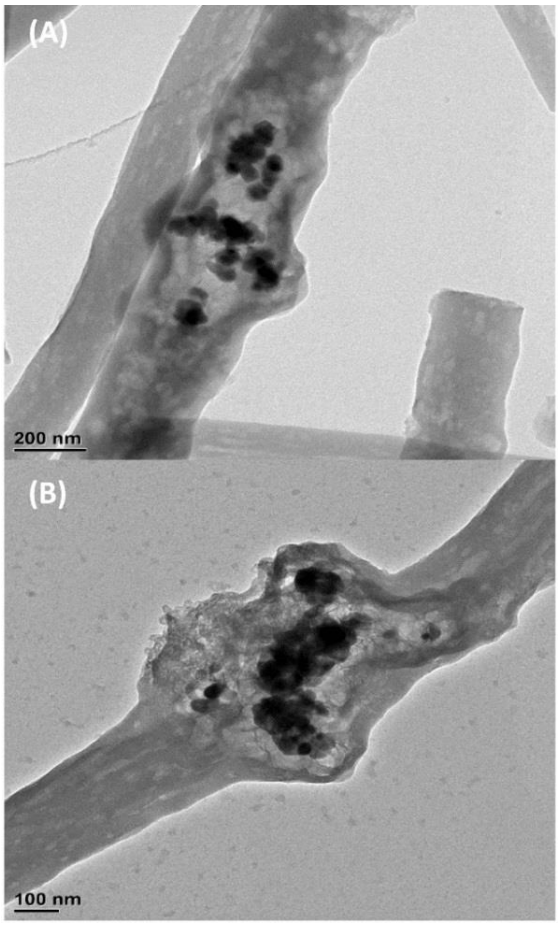

Figure 4. TEM images of SnSb@C nanofibers prepared from precursor with ATO:PAN ratio of 0.5:1.

SnSb nanoparticles formed in-situ during carbonization are nano-sized and can facilitate a shorter lithium ion diffusion path length. These SnSb nanoparticles are encapsulated inside the carbon nanofibers. Encapsulating high-capacity active materials into a porous carbon matrix is a common practice for accommodating their large volume changes for the purpose of improving the cycling performance.[19–21] For example, Yan *etal*. produced Sn-encapsulated porous carbon nanofiber composite by single-nozzle electrospinning and the material exhibits excellent reversible capacities, cycling performance, and rate capability due to the multichannel and porous structure.[19] It is also seen from Figure 4 that a porous structure has been formed around SnSb nanoparticles inside the carbon nanofiber matrix, which is mainly resulted from the decomposition of PMMA. The porous structure can help buffer the large volume changes of SnSb nanoparticles during sodiation-desodiation process and prevent the fracture of the carbon nanofiber matrix.

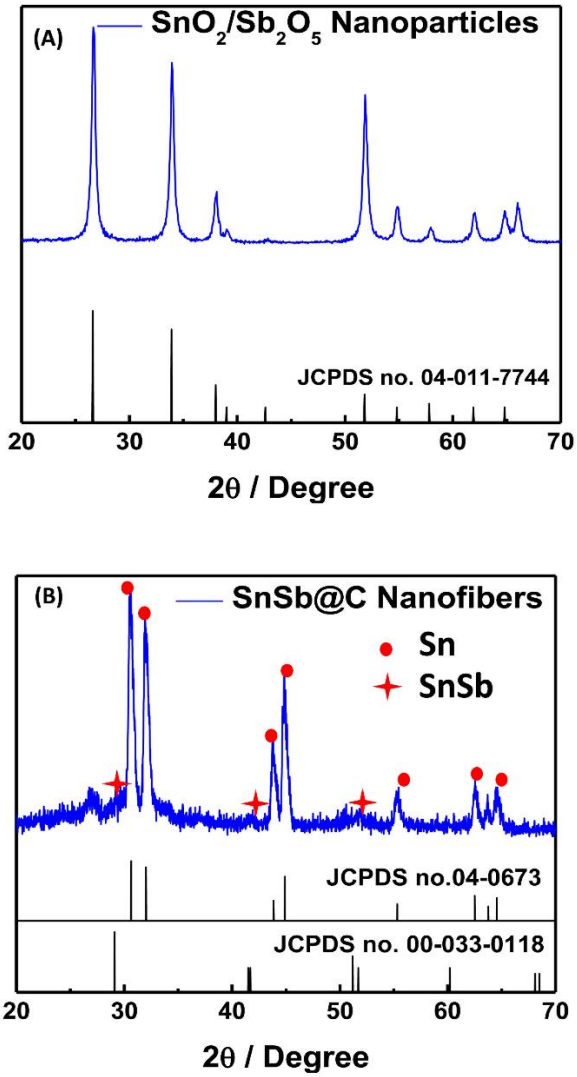

Figure 5. XRD patterns of (A) ATO nanoparticles, and (B) SnSb@C nanofibers prepared from precursor with ATO:PAN ratio of 0.5:1.

XRD patterns of ATO precursor nanoparticles and SnSb@C nanofibers are shown in Figure 5. In Figure 5A, characteristic peaks are observed at 26.4°, 33.8°, 38.0°, 39.0°, 51.7° 61.9°, 64.8°, and 66.0° for ATO nanoparticles. In Figure 5B, the peaks at 30.7°, 32.0°, 44.1° and 45.1° can be attributed to metallic Sn phase while the peaks at

29.1°, 41.5°, 41.7°, 51.2°, and 60.2° can be ascribed to the SnSb phase, indicating the reduction of the ATO nanoparticles and the formation of Sn and SnSb phases. Due to the small content of Sb_2O_5 in the ATO precursor (7-11%), the SnSb phase shows weak peaks in the XRD pattern. Hence, during the thermal treatment, the ATO nanoparticles were transformed to SnSb nanoparticles, consisting of Sn and SnSb phases, by using pyrolytic carbon as a reduction agent under the inert argon atmosphere.

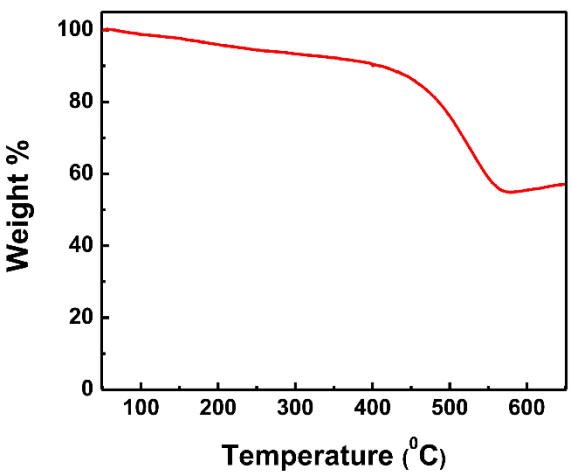

Figure 6. TGA curve of SnSb@C nanofibers prepared from precursor with ATO:PAN ratio of 0.5:1.

In order to determine the carbon content in the composite, TGA test was conducted in air (Figure 6) and the result shows a carbon content of 40% for SnSb@C nanofibers prepared from precursor with ATO:PAN ratio of 0.5:1. An elemental analysis was also conducted and it is found that there are 52.8% SnSb, 41.1% carbon, 1.0% hydrogen, and 5.1% nitrogen in the SnSn@C nanofiber composite prepared with ATO:PAN ratio of 0.5:1.

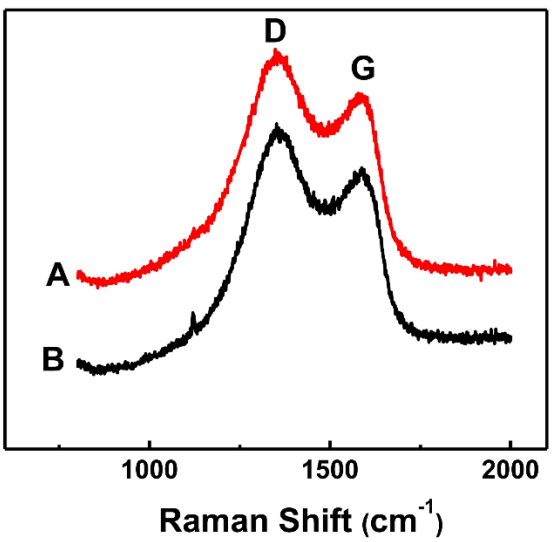

Figure 7. Raman spectra of (A) carbon nanofibers, and (B) SnSb@C nanofibers prepared from precursor with ATO:PAN ratio of 0.5:1.

Figure 7 compares the Raman spectra of carbon nanofibers and SnSb@C nanofibers (ATO:PAN = 0.5:1). For both nanofibers, there are two distinct peaks at 1600 (G band) and 1350 cm^{-1} (D band), which are associated with the vibration of sp^2 bonded carbon in planar sheets and the presence of defects and disordered carbon,

respectively. The intensity ratios of the D band and G band, *i.e.*, I_D/I_G ratio, is often used to assess the disorder feature of carbon materials. From Figure 7, it is seen that the I_D/I_G ratios of carbon nanofibers and SnSb@C nanofibers are 1.18 and 1.19, respectively. The relatively high I_D/I_G ratios suggest the disordered nature of the carbon structure in both carbon nanofibers and SnSb@C nanofibers.

Electrochemical Evaluation

Figure 8 shows the cyclic voltammetry (CV) test results of SnSb@C nanofibers with different ATO:PAN ratios. In Figure 8A, the electrochemical behavior of pure carbon nanofibers (*i.e.*, ATO:PAN = 0:1) was studied. In the first reduction scan, the peak shown at 0.5V is due to the formation of solid electrolyte interface (SEI) on the surface of carbon nanofibers. The sodiation process in the carbon nanofibers mainly occurs at 0.02V which corresponds to the peak in the Figure 8A. For SnSb@C nanofibers prepared from precursor with ATO:PAN ratio of 0.5:1, the peak at 0.35V in the first cycle can be mainly ascribed to the irreversible reaction that produces the SEI film.

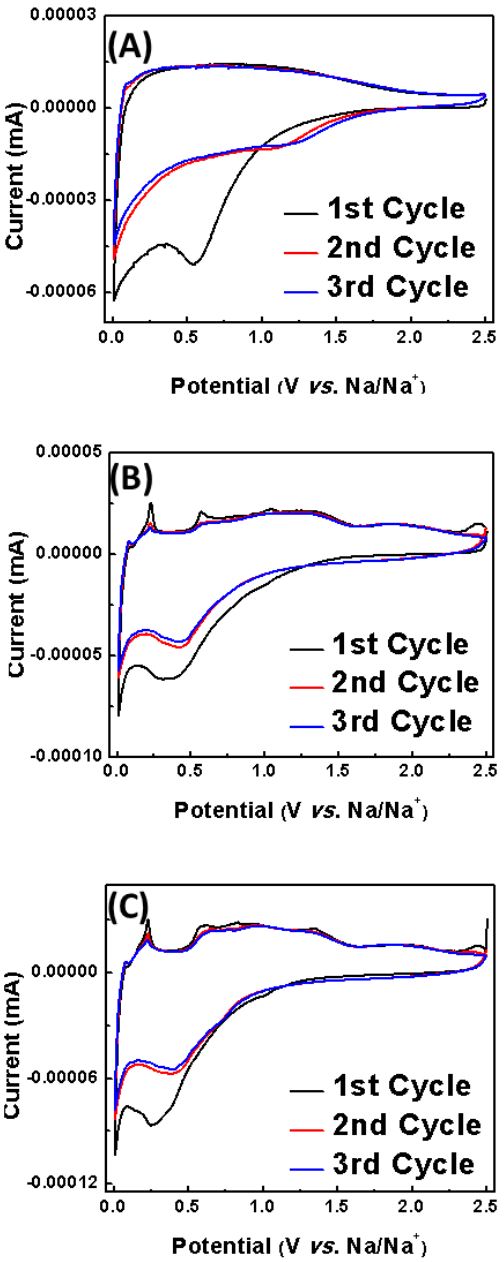

Figure 8. Cyclic voltammetry curves of SnSb@C nanofibers prepared from precursor with different ATO:PAN ratios: (A) 0:1, (B) 0.5:1, (C) 1:1.

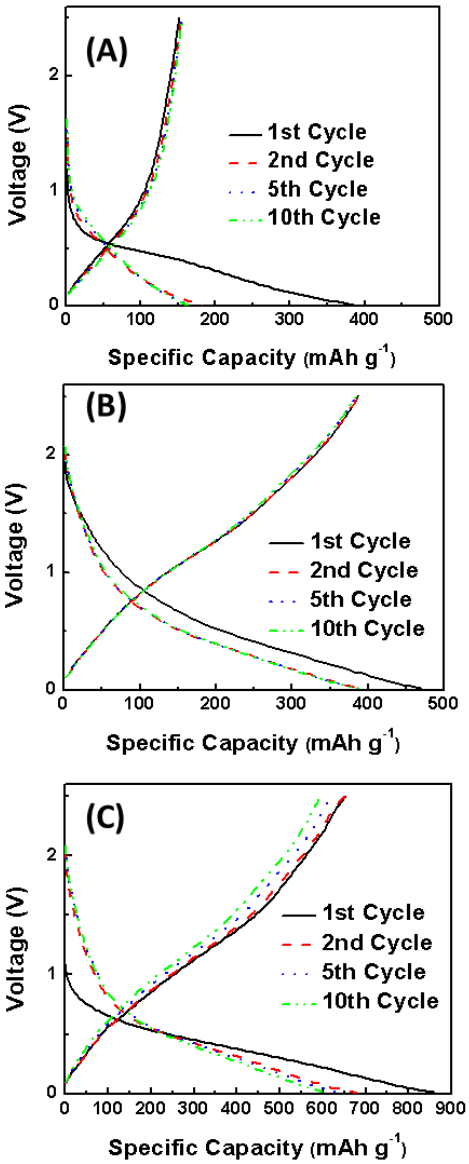

Figure 9. Charge-discharge curves of SnSb@C nanofibers prepared from precursors with different ATO:PAN ratios: (A) 0:1, (B) 0.5:1, (C) 1:1.

After the first cycle, the reductive peak at 0.02 can be assigned to the Na-ion insertion into the carbon matrix while that at 0.5V is for Na-ion insertion to the SnSb nanoparticles to form $Na_{15}Sn_4$ and Na_3Sb. Correspondingly, the oxidative peaks at 0.1V, 0.5V and 0.6V indicated the Na-ion extraction from carbon matrix, $Na_{15}Sn_4$ phase, and Na_3Sb phase[16]. With the ATO:PAN ratio increased to 1:1, the electrochemical behavior of the electrode does not change and the oxidative peaks at 0.1V, 0.5V and 0.6V and reductive peaks at 0.02 and 0.5V still can be seen in the CV curve.

Figure 9 shows the charge-discharge curves of SnSb@C nanofibers prepared from precursors with different ATO:PAN ratios. The current density used was 500 mA g^{-1}. For the pure carbon nanofibers (ATO:PAN = 0:1), an initial capacity of 380 mAh g^{-1} and reversible capacity of 161 mAh g^{-1} can be obtained and during the first cycle, a discharge plateau at 0.5V can be observed which relates to the SEI formation and corresponds to the peak observed in the CV curve (Figure 8). The initial capacity loss of carbon nanofibers is large due to the formation of SEI film and the irreversible reactions between sodium and surface functional groups. The large initial capacity loss leads to low coulombic efficiency for carbon nanofibers in the initial cycle.[10,22] The addition of

ATO reduces the content of carbon in the entire electrode, which might lead to reduced initial capacity loss and increased coulombic efficiency. From Figure 9, it is seen that for SnSb@C nanofibers prepared from precursor with ATO:PAN ratio of 0.5:1, the specific discharge capacity at the first cycle is 470 mAh g^{-1}, with a Coulombic efficiency of 82.6%. The irreversible capacity loss in the first cycle is mainly attributed to the reduction of the electrolyte for SEI formation on the surface of the electrode during the first discharge step.[23] This high Coulombic efficiency can be attributed to the proper size of the nanoparticles and the well-protected nanoparticles by carbon nanofiber matrix. It is known that smaller particles have larger surface area which will promote the formation of the SEI leading to lower Coulombic efficiency during the first charge-discharge process. The size of the obtained Sn and SnSb alloy nanoparticles are around 50 nm which is beneficial to the formation of SEI and increase of the first Coulombic efficiency.[24,25] For the SnSb@C nanofibers prepared from precursor with ATO:PAN ratio of 1:1, the specific discharge capacity is 859 mAh g^{-1} at the first cycle and the Coulombic efficiency is 76.0%. The initial capacity loss of SnSb@C nanofibers prepared with a lower ATO:PAN ratio of 0.5:1 is much smaller than that of SnSb/C nanofibers prepared with a higher ATO:PAN ratio of 1:1. From the subsequent discharge curves, the plateau at 0.5V indicates the Na-ion insertion into SnSb nanoparticles, which corresponds to the peak at 0. 5V in the CV curve. After the 2nd cycle, the specific capacity tends to stabilize and the Coulombic efficiency increases to above 95.0%.

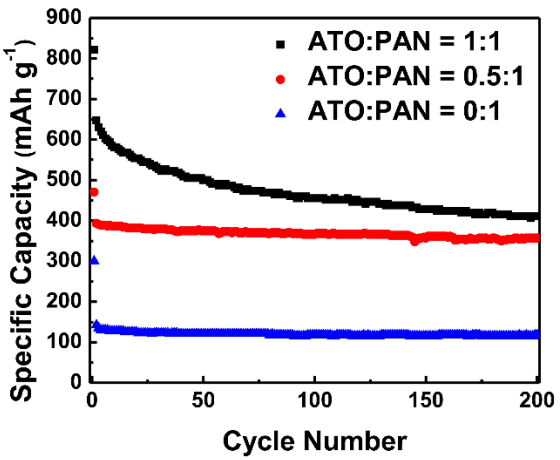

Figure 10. Cycling performance of SnSb@C nanofibers prepared from precursors with different ATO/PAN ratios under current density of 500 mA g^{-1}.

The cycling performance of SnSb@C nanofibers prepared from precursors with different

ATO:PAN ratios were also evaluated at a current density of 500 mA g^{-1} and the results are shown in Figure 10. Pure PAN-derived carbon nanofibers (ATO:PAN = 0:1) show a capacity of 130 mAh g^{-1} in most cycles and this capacity value is significantly lower than those of SnSb@C nanofibers prepared with ATO:PAN ratios of 0.5:1 and 1:1. This indicates that the majority of the capacity of SnSb@C nanoparticles is provided by SnSb nanoparticles. From Figure 10, it is seen that when the ATO:PAN is 0.5:1, a reversible capacity of 380 mAh g^{-1} is achieved after the first cycle, and the capacity decreases gradually to 356 mAh g^{-1} at the 200th charge-discharge cycle, indicating a capacity retention of as high as 93.7%. When the ATO:PAN ratio is 1:1, a high initial capacity is expected due to the presence of higher amount of SnSb nanoparticles. A high reversible capacity of 649 mAh g^{-1} is achieved after the first cycle, however, the capacity reduces to 410 mAh g^{-1} at the 200th cycle, indicating a capacity retention of 63.2%. Therefore, the capacity retention of SnSb@C nanofibers prepared with ATO:PAN ratio of 1:1 is lower than that of SnSb@C nanofibers with ATO:PAN ratio of 0.5:1. This is because in SnSb@C nanofibers prepared with ATO:PAN ratio of 1:1, some SnSb nanoparticles may not be completely encapsulated inside the carbon nanofiber matrix and the volume change of unprotected SnSb nanoparticles is not effectively buffered during the sodiation-desodiation process, resulting in larger capacity loss. The excellent cycling behavior for SnSb@C nanofibers prepared with ATO:PAN ratio of 0.5:1 can be attributed to both the buffering effect of carbon nanofiber matrix and the void space surrounding the SnSb nanoparticles.

The rate capability of SnSb@C nanofibers prepared from precursor with ATO:PAN ratio of 0.5:1 was studied by increasing the current density sequentially from 50 mA g^{-1} to 100 mA g^{-1}, 200 mA g^{-1}, 500 mA g^{-1}, and 1 A g^{-1}, respectively (Figure 11).

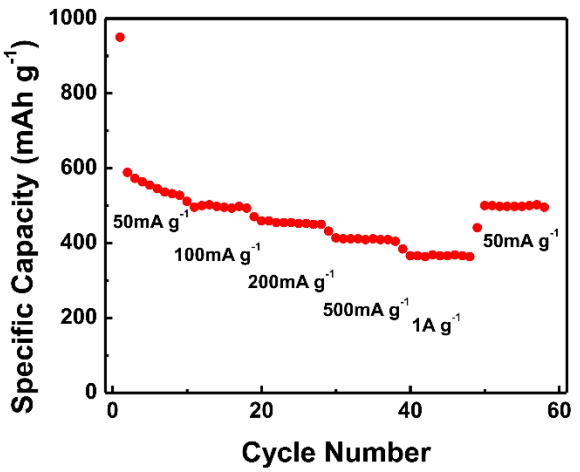

Figure 11. Rate capability of SnSb@C nanofibers prepared from precursor with ATO:PAN ratio of 0.5:1 from 50 to 1000 mA g^{-1}.

It is seen that at 50 mA g^{-1}, the SnSb@C nanofibers deliver a capacity of 590 mA g^{-1}. As the current density increases, the capacity decreases gradually, however, a relatively high capacity of 370 mAh g^{-1} is still maintained at 1 A g^{-1}, corresponding to a capacity retention of 62.7% with respect to the capacity at 50 mA g^{-1}. When the current density returns back to 50 mA g^{-1} after 50 cycles, a capacity as high as 560 mAh g^{-1} is restored, revealing a good reversibility, which confirms the stable structure of SnSb@C nanofibers. This excellent rate capability can be attributed to the binary alloy of SnSb which can act as the buffer to alleviate the volume change for each other and the porous carbon nanofiber structure, which can accommodate the volume change of SnSb nanoparticles while providing conductive pathways for both electrons and Na ions.[26] Moreover, the porous structure around the nanoparticles can also facilitate the diffusion of the electrolyte and Na ions, which promotes the kinetics of electrode reactions.

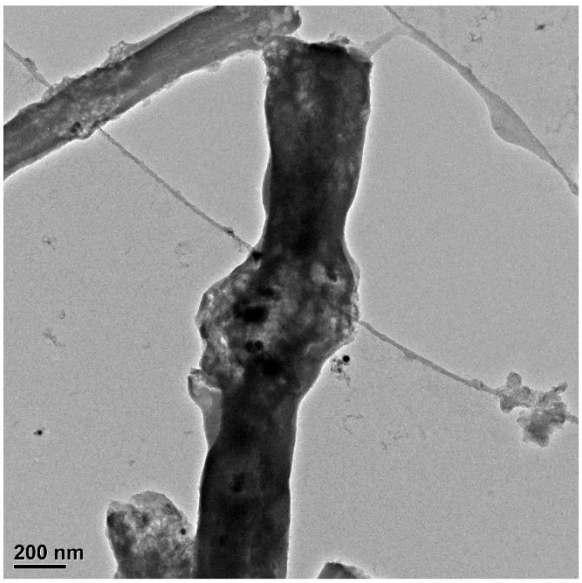

Figure 12. TEM image of SnSb@C nanofibers after 200 charge-discharge cycles under the current density of 500mA g^{-1}.

In order to investigate the morphology change of SnSb@C nanofibers, the cell was disassembled and examined by TEM after 200 charge-discharge cycles (Figure 12). It is seen that the spherulitic

structure of SnSb nanoparticles was maintained and most particles were still encapsulated in the carbon nanofiber matrix, suggesting that the pulverization and aggregation of SnSb nanoparticles were contained inside the carbon nanofiber matrix.

Conclusion

In this work, ATO nanoparticles, PAN and PMMA were utilized to produce a SnSb nanoparticle-filled porous carbon fiber composite for use as the anode material in sodium-ion batteries. The morphology, active material content and electrochemistry performance were evaluated by XRD, SEM, TEM, and elemental analysis. The uniform and stable porous structure, confirmed by the SEM and TEM images, can provide space and confinement for SnSb nanoparticles and buffer the volume expansion-contraction during repeated charge-discharge cycling. The high capacity and excellent cycling performance under high current density demonstrated the good electronic contact from carbon nanofibers during cycling and the excellent stability of the active material.

Acknowledgements

This research was supported by National Science Foundation under Award Number CMMI-1231287, and Zhejiang Provincial Natural Science Foundation under Award Number LY12E03005.

References

(1) Chevrier, V. L.; Ceder, G. *J. Electrochem. Soc.* **2011**, *158*, A1011.

(2) Wang, Z.; Wang, Z.; Liu, W.; Xiao, W.; Lou, X. W. (David). *Energy Environ. Sci.* **2013**, *6*, 87.

(3) Zhu, Y.; Han, X.; Xu, Y.; Liu, Y.; Zheng, S.; Xu, K.; Hu, L.; Wang, C. *ACS Nano* **2013**, *7*, 6378.

(4) Kim, S.-W.; Seo, D.-H.; Ma, X.; Ceder, G.; Kang, K. *Adv. Energy Mater.* **2012**, *2*, 710.

(5) Lu, Y.; Zhang, S.; Li, Y.; Xue, L.; Xu, G.; Zhang, X. *J. Power Sources* **2014**, *247*, 770.

(6) Kim, H.; Kim, D. J.; Seo, D.; Yeom, M. S.; Kang, K.; Kim, D. K. *Chem. Mater.* **2012**, *24*, 1205.

(7) Kim, D.; Kang, S.-H.; Slater, M.; Rood, S.; Vaughey, J. T.; Karan, N.; Balasubramanian, M.; Johnson, C. S. *Adv. Energy Mater.* **2011**, *1*, 333.

(8) Stevens, D. A.; Dahn, J. R. *J. Electrochem. Soc.* **2001**, *148*, A803.

(9) Lin, Y.-M.; Abel, P. R.; Gupta, A.; Goodenough, J. B.; Heller, A.; Mullins, C. B. *ACS Appl. Mater. Interfaces* **2013**, *5*, 8273.

(10) Fu, L.; Tang, K.; Song, K.; van Aken, P. A; Yu, Y.; Maier, J. *Nanoscale* **2014**, *6*, 1384.

(11) Wenzel, S.; Hara, T.; Janek, J.; Adelhelm, P. *Energy Environ. Sci.* **2011**, *4*, 3342.

(12) Xue, L.; Xia, X.; Tucker, T.; Fu, K.; Zhang, S.; Li, S.; Zhang, X. *J. Mater. Chem. A* **2013**, *1*, 13807.

(13) Wang, Y.; Lee, J. Y. *Angew. Chem. Int. Ed. Engl.* **2006**, *45*, 7039.

(14) Lee, K. T.; Jung, Y. S.; Oh, S. M. *J. Am. Chem. Soc.* **2003**, *125*, 5652.

(15) Qin, J.; He, C.; Zhao, N.; Wang, Z.; Shi, C.; Liu, E.-Z.; Li, J. *ACS Nano* **2014**, *8*, 1728.

(16) Xiao, L.; Cao, Y.; Xiao, J.; Wang, W.; Kovarik, L.; Nie, Z.; Liu, J. *Chem. Commun. (Camb).* **2012**, *48*, 3321.

(17) Yamamoto, T.; Nohira, T.; Hagiwara, R.; Fukunaga, A.; Sakai, S.; Nitta, K.; Inazawa, S. *J. Power Sources* **2012**, *217*, 479.

(18) Palomares, V.; Serras, P.; Villaluenga, I.; Hueso, K. B.; Carretero-González, J.; Rojo, T. *Energy Environ. Sci.* **2012**, *5*, 5884.

(19) Yu, Y.; Gu, L.; Wang, C.; Dhanabalan, A.; van Aken, P. a; Maier, J. *Angew. Chem. Int. Ed. Engl.* **2009**, *48*, 6485.

(20) Yu, Y.; Gu, L.; Zhu, C.; van Aken, P. a; Maier, J. *J. Am. Chem. Soc.* **2009**, *131*, 15984.

(21) Fu, K.; Xue, L.; Yildiz, O.; Li, S.; Lee, H.; Li, Y.; Xu, G.; Zhou, L.; Bradford, P. D.; Zhang, X. *Nano Energy* **2013**, *2*, 976.

(22) Wang, Z.; Qie, L.; Yuan, L.; Zhang, W.; Hu, X.; Huang, Y. *Carbon N. Y.* **2013**, *55*, 328.

(23) Idota, Y.; Kubota, T.; Matsufuji, A.; Maekawa, Y.; Miyasaka, T. *Science* **1997**, *276*, 1395.

(24) Aricò, A. S.; Bruce, P.; Scrosati, B.; Tarascon, J.-M.; van Schalkwijk, W. *Nat. Mater.* **2005**, *4*, 366.

(25) Trifonova, A. *Solid State Ionics* **2004**, *168*, 51.

(26) Wachtler, M.; Winter, M.; Besenhard, J. O. *J. Power Sources* **2002**, *105*, 151.